Advances in Remote Sensing, 2023, 12, 1-28
https://www.scirp.org/journal/ars
ISSN Online: 2169-2688
ISSN Print: 2169-267X

Snowmelt Flood Mapping and Land Surface Short-Term Dynamics Assessment in a "Before-During-After" Scenario Based on Radar and Optical Satellite Imagery: Case Study Around the Lewisville Lake (Dallas/Fort Worth Metropolitan, Texas, USA)

Alfred Homère Ngandam Mfondoum[1,2*], **Roseline Batcha**[2]

[1]Stats'NMaps, Private Consulting Firm, Dallas, USA
[2]Department of Geography, University of Yaoundé I, Yaoundé, Cameroon
Email: *stats.n.maps.expertise@gmail.com, alfred.homere@gmail.com, batcharoseline@gmail.com

How to cite this paper: Ngandam Mfondoum, A.H. and Batcha, R. (2023) Snowmelt Flood Mapping and Land Surface Short-Term Dynamics Assessment in a "Before-During-After" Scenario Based on Radar and Optical Satellite Imagery: Case Study Around the Lewisville Lake (Dallas/Fort Worth Metropolitan, Texas, USA). *Advances in Remote Sensing*, **12**, 1-28.
https://doi.org/10.4236/ars.2023.121001

Received: November 7, 2022
Accepted: February 27, 2023
Published: March 2, 2023

Abstract

The main goal of this study has been to map flood and assess land surface short-term dynamics in relation with snowy weather. The two recent snowfall events, which happened in, February 14th and 15th, of year 2021, and February 3rd and 4th, of year 2022, were chosen. A pre-analysis correlation was assumed between, the snow events, recurrency of floods, and changes in the land surface characteristics (*i.e.*, wetness, energy, temperature), in a "Before-During-After" scenario. Active and passive microwave satellites data such as, Sentinel-1 synthetic aperture radar (SAR), Sentinel-2 multispectral instrument (MSI) and Landsat-9 Operation Land Imager-2/Thermal Infrared Sensors-2 (OLI-2/TIRS-2), as well as cloud databased global models for water and urban layers were used. The first step of processing was thresholding of SAR image, at 0.25 cutoff, based on bimodal histogram distribution, followed by the change analysis. The following processing consisted in the images transformation, by computing the tasseled cap transformation wetness (TCTw) and the surface albedo on MSI image. In addition, the land surface temperature (LST) was modeled from OLI-2/TIRS-2 image. Then, a 5th order polynomial regression was computed, between TCTw as dependent variable and, albedo and LST as independent variables. As a first result, an area of 5.6 km^2 has been mapped as recurrently flooded from the two years assessment. The other output highlighted a constant increase of wetness (TCTw), considered most influential on land surface dynamics, comparatively to energy exchange (albedo) and temperature (LST). The "After" event dependency between the three indicators was highest, with a correlation coefficient, $R^2 = 0.682$, confirming the persistence of wetness after-snowmelt. Validation over topographic layers confirmed that, recurrently flooded areas are mostly distributed on, lowest valley depth points, farthest distances from channel network (*i.e.*, from perennial waters), and lowest relative slope position areas. Whereas, 88.9% of the validation sampling were confirmed in the laboratory, and 86.7% of urban validation points were assessed as recurrently flooded when combining pre-/post-fieldwork campaign.

Keywords

Snowmelt Flood, Short-Term Dynamics, Radar, Optical, Lewisville Lake

1. Introduction

Human life and activities are deeply conditioned by seasonal or permanent weather's conditions, depending on the geolocation. Snow especially has a large-scale cooling effect on various components of mid and high latitudes specifically, and on the Earth system globally, like hydrology, ecology, climatology, global energy cycle, water and carbon cycles, due to the large seasonal variability [1] [2]. The changing snow regime has major consequences for terrestrial ecosystems, including increasing hazards for regional communities [3].

Earth observatory sciences (EOs) have been proven efficient in studying and spatializing heat or cold environmental weathers consequence. The progresses of snow and ice remote sensing specifically in last decades has opened up opportunities for accurate and diversified applications in view of better mitigations. Most applications are usually referred as land surface models, with various tools that have been efficient and improved through time. They have been reviewed in this study according to directly perceptible impacts (e.g., cover), or less visible one's influence with a still direct disastrous impact (e.g., energy).

The snow extreme wetness, with a direct impact in permanently and seasonally exposed areas, has motivated several studies depending on the season length. Amongst other, the snow cover distribution and surrounding land covers have been mapped, using the snowmap algorithm [4]. Originally developed for MODIS sensor, and used by a bunch of other sensors, snowmap is based on the reflectance of visible and infrared radiation, to calculate the normalized difference snow index (NDSI). This algorithm only works for pixels with at least a 50% snow-cover fraction [5]. The fractional snow-cover has been explored by thresholding the NDSI [6], or using a linear spectral mixture analysis applied to hyperspectral imaging spectrometer data [7]. While the wet and dry snow have been separated using active and passive microwave data [8] [9] [10].

Other studies focused on the snow phenology. New metrics such as daily (diurnal) freeze-thaw (FT) dynamics, mean melt onset date (MMOD), snow cover depletion date (SO), and snowmelt duration (SMD) were introduced [3]. The internal microphysics property of snow was also studied inside a snowpack, which consists of air, ice and in some cases liquid water [11]. Whereas, the insulating properties of snow have been analyzed in relation with soil carbon [12].

Macro/micro-climate interactions have been analyzed at regional or local scales, through themes of surface energy budget, albedo or Land Surface Temperature (LST). For example, the relation between drifting-snow particles with the lower atmosphere and the surface energy budget (SEB) [13]. The albedo estimation from snow has especially been mapped with generalized or specific models [14] [15]. Amongst others, the broadband albedo of Landsat bands [16], MODIS Bi-directional Reflectance Distribution Function/Albedo Product model inversion [17] or compared *in situ* and MODIS albedo values agreement [18] models have been efficient. Albedo dynamics had also been studied inside a snowpack, analyzing its relation with the snowpack microphysics [11]. Some other models have been focusing on the snow cover dynamics in direct relations with LST [19] [20], or general land cover, because changes in snow depth (SD) influences mainly the vegetation growth [21] [22].

Besides, the snow on the ground is particularly relevant for the management of water resources, due to the direct impact of its melting on nearby streams [9]. The snow cover is then important for regional or local water availability, as snowmelt immediately affects the hydrological cycle, with water raise of lakes, runoff dynamic of rivers, and groundwater recharge, especially in middle and high latitudes [23] [24]. This importance is tightly dependent on the snow cover variability both in time and space [25], as well as on scale and amount melted. Whereas, the cover and melting relation with surface water dynamics is technically assessed through the snow water equivalent (SWE) [26].

On the other hand, this management includes natural hazard risks. The snow melting is responsible for avalanche and hydrology that are the most directly related processes in this case. Therefore, sudden melt [27], flooding and run-off [28] [29], have been modeled using advanced processing, to prevent and mitigate related hazards. Flood and surface dynamics are especially targeted by this paper.

The Dallas/Fort Worth (DFW) metropolitan area (Texas, USA) recently recorded two important snowfalls[1]. The first event took place between February 14th and 15th, of 2021, reaching 5 inches (12.7 cm) of snow. The second one occurred between February 3rd and 4th, of 2022, reaching between 1.7 inches and 2.5 inches (4.3 - 6.3 cm) of sleet and snow, going up to 6 inches (15.2 cm) per local measurements (**Figure 1**). However, these snowfalls are way below the "*snowpocalypse*"[2] that occurred in February 10th of 2010, reaching an official 12.5 inches (31.8 cm). This latter is known since then as the heaviest single-day snowfall on record. One direct consequence of these conditions, is usually the slowdown of activities and traffic, as roads and buildings are directly impacted (**Figure 2** and

[1] https://www.weather.gov/fwd/dmosnow

[2] https://www.onlyinyourstate.com/texas/dallas-fort-worth/massive-blizzard-in-dallas-fort-worth-in-snow-in-2010/

Figure 1. In situ measurements. Flowermound for February 14th, of 2021 (left) and Lewisville for February 3rd, of 2022 (Right).

Figure 2. Preview of affected human settlements/environment for selected sites in DFW Metropolitan during and after the snowfall of 2022. From left to right: A residential (apartments) complex at Lakeside by "Golf Lakes Trail 9600" (February 3rd); the bridge on "Walnut Hill Lane" near Fair Oaks Park (February 3rd); the lake below the bridge at Fair Oaks Park (February 4th); unmelted snow on a lawn in Addison at "16479 Dallas Parkway" (February 8th).

Supplemental material). Whereas the instant freezing of lakes and some running waters is noticeable.

Although these significant impacts in DFW metropolitan, practically, snowfalls are sporadic, short (one or two days) and punctual, thanks to the humid subtropical climate (mean annual: precipitations = 1538 mm; temperature = 24.5˚C) [30]. The Denton County cities' council (especially of Lewisville), have been mapping and identifying the flooded areas with (potential) threats related. Nevertheless, specific tools and metrics can raise concerns about the last statement. From the official records, the snow water equivalent (SWE-*Inch*) and the snow depth (*Inch*) are positively correlated, and always highest than the snow density (*Inch*) and the melt rate (*Inch/hour*). For the studied events, the melt rate especially was very slow, extending over three to four days after the snowfalls (**Figure 3** and **Supplemental material**), with a non-significant threatening effect on lake and streams level raise. However, when considering natural features such as, the type of soils (loamy and clayey porous sands and tight clays)[3] enabling slow infiltration and stagnation, presence of grassy vegetation, relatively flat terrain with low slopes, and imperviousness sprawl consequent to urbanization, it is interesting to identify areas presenting potential risk of snowmelt flooding, in case of unpredicted huge falls.

This paper focuses on the two above mentioned recent snowfalls impact over urbanized and natural land covers. One goal is to map the recurrently flooded

[3]https://soilseries.sc.egov.usda.gov/OSD_Docs/L/LEWISVILLE.html#:~:text=The%20Lewisville%20series%20consists%20of,914%20mm%20(35.98%20in.)

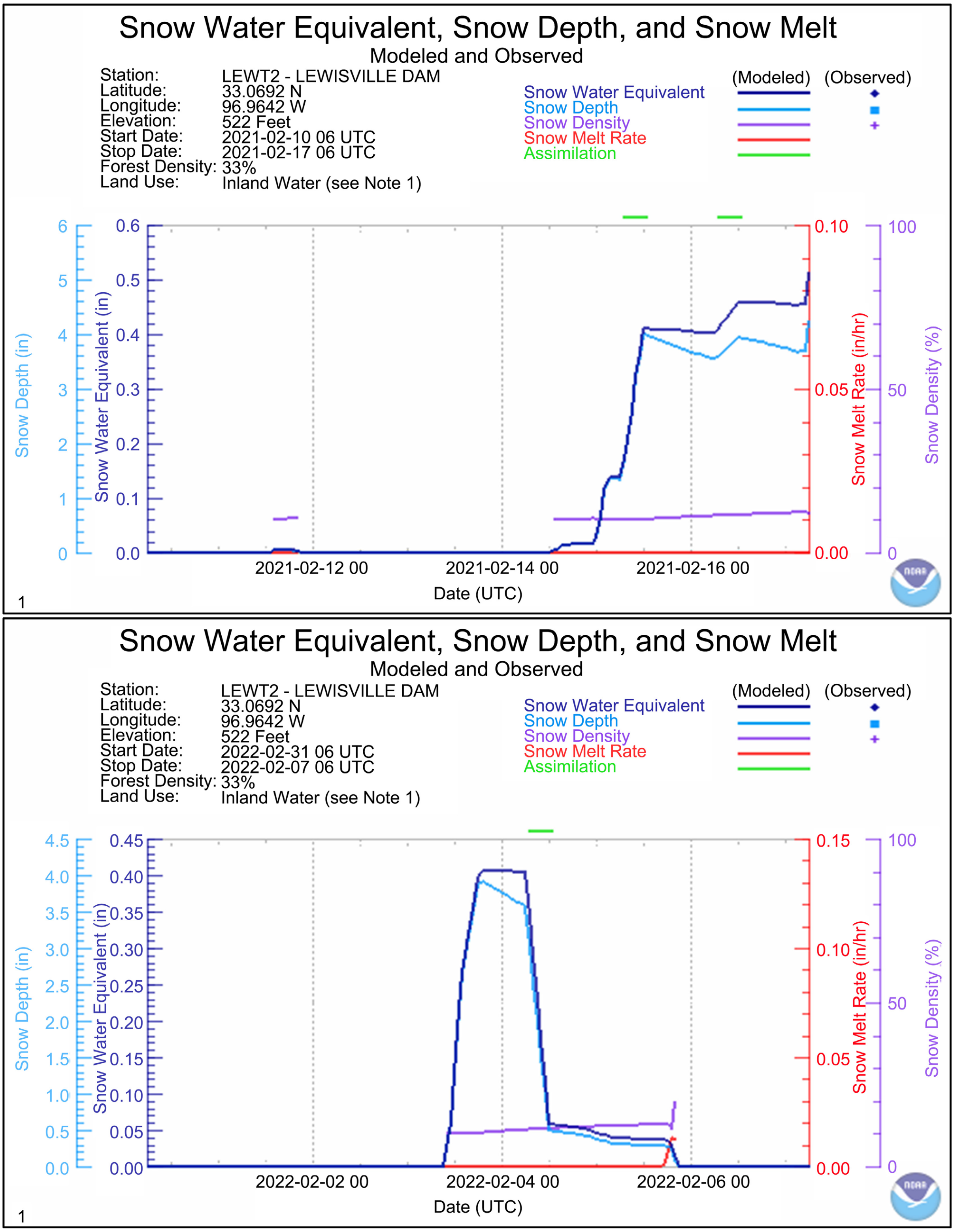

Figure 3. Selected snow metrics before and after snowfalls in 2021 and 2022 (Source: https://www.weather.gov/fwd/dmosnow).

areas after snowmelt around Lewisville Lake, assuming a more direct threat in case of unexpected huge snowfall similar to February 10th, of 2010. Another goal is to characterize the state of land surface, for a better assessment of the implications on natural features and human settlements. Afterward, a cause-and-effect relation between flood and land surface dynamics is established. To clear up any ambiguity, the study does not pretend to substitute advanced models employing very-high spatial and spectral resolution images or up-to-date monitoring processes supported by real-time computations as mentioned above. The proposed methodology is rather a, from an easy-to-go perspective, with freely available data and opensource software/coding. Therefore, this is a quick modelling process, intended to support forecasts and warnings of data-limited meteorologists, as well as planning actions in regard to snow events, using the case of Denton's County.

2. Materials and Methods

2.1. Study Area

The study was conducted on a subset of 233.237 km^2, embedding Lewisville Lake on the Elm Fork of the Trinity River, and nearest built-up. It is located between North latitudes 33˚0'0" - 33˚20'0", and West longitudes 97˚48'0" - 97˚55'0", with low and smooth altitudes between 130 - 225 m (**Figure 4**). The total drainage area is extended on 4300 km^2 with several other streams. Thanks to its different usages, the Lewisville Lake is solicited by at least twenty-five major cities located within the "Trinity River Watershed" [31]. The water level monitoring and quality control of the dam is then of a major importance, as the population growth rate keeps increasing (example of the city of Lewisville: 2% in 2020; 21.77% since 2010)[4]. Whereas the urbanization and imperviousness replace soils and vegetation [32].

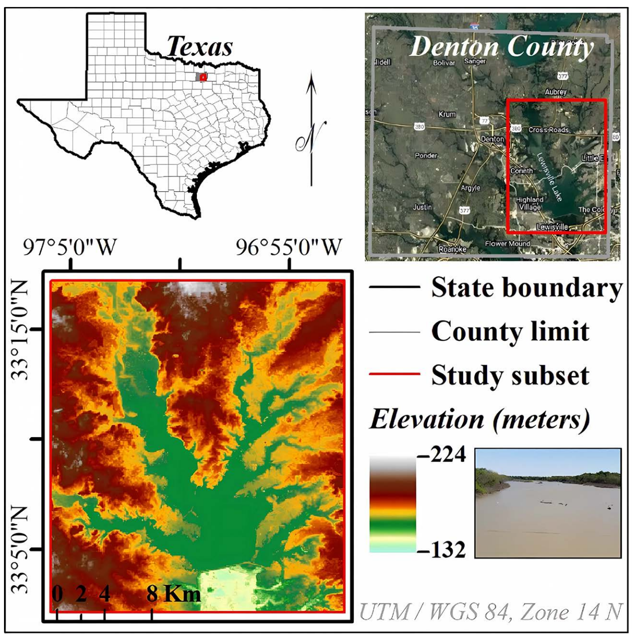

Figure 4. Study location and partial view of the Lewisville Lake from the highway "U.S.380West – West University Drive".

[4]https://worldpopulationreview.com/us-cities/lewisville-tx-population

2.2. Work Environment and Tools

Processing phases were conducted alternatively between the cloud environment and desktop tools. Google Earth Engine (GEE) platform was used for cloud computing. This is a geospatial image data viewer with access to a large set of global and regional datasets, which supports big data computations, in terms of scale and/or time lapse coverage [33]. Simple JavaScript codes were successfully implemented for semi-automatic preprocessing and processing. While offline tools such as, SNAP 9.0.0, SAGA-GIS version 8.0.1, ArcGIS version 10.8.2, Erdas Imagine 2020 version 16.6.0.1366 and XLStats version 2020.1.64570, helped to complete analyses, compute statistics and proceed with maps layout.

2.3. Data Overview and Preprocessing

Active microwave (AM) and passive microwave (PM) data and their recording respective, have their advantages and drawbacks in recognizing snow extent, snow depth (SD) and snow water equivalent (SWE) [34]. They provide a large and continuous database at different scales. In this study, both AM and PM data were used, specifically, Sentinel-1 Synthetic Aperture Radar (S1-SAR), Sentinel-2 Multispectral Instrument (S2-MSI) and Landsat-9 Operation Land Imager-2/Thermal Infrared Sensors-2 (OLI-2/TIRS-2). All the data were loaded to the GEE interface from its cloud geodatabase for partial or complete processing.

2.3.1. Synthetic Aperture Radar (SAR) Data

SAR data of the Sentinel-1 mission offers a good freely available alternative for wet snow cover mapping [25]. At high-latitudes, Sentinel-1 provides a 3-5-days (ground track) revisit cycle, acquired in different swath modes among which the Interferometric Wide (IW) that was used here, with a 250-km swath width, a 20 × 22 m spatial resolution, and burst synchronization for interferometry[5]. The format is the ground range detected (GRD), a Level-1 product, generated in 16-bit unsigned integer. The central band (C-Band), which operates at central frequency of 5.405 gigahertz (GHz) was selected, because it is not hindered by atmospheric effects and has the capacity of imaging through clouds and rain showers [35]. C-Band (≈5.6 cm) wavelength is provided at single-polarization (σ_{HH}, σ_{VV}) or dual-polarization ($\sigma_{HH} + \sigma_{HV}$ and $\sigma_{VV} + \sigma_{VH}$). After display, visual inspection and simulations on the "During" step image, the cross-polarization "Vertical Transmission-Horizontal Reception" (VH) was selected to move forward. Visually, VH, reflected the sharpest signal contrast between whiter land cover, *i.e.*, snow, and darker ones. In this regard and per the existing literature, vertically polarized data are more sensitive to the snow volume and are therefore capable of mapping shallow snow cover, while horizontally polarized data untangle confusion between snow and underlying dry soils [34] [36] [37]. Then their cross-combination is advantageous for snow mapping. According to the timeline targeted, two (02) images were obtained for 2021 ("Before-After") and three (03) for 2022 ("Before-During-After") (**Table 1** & **Table 2**).

[5]https://sentinels.copernicus.eu/web/sentinel/user-guides/sentinel-1-sar/definitions

Table 1. Identification of SAR (GEE JSON's format).

GRD ID	Acquisition
S1A_IW_GRDH_1SDV_20210209T002752_20210209T002817_036506_044964_33AC	11/02/2021
S1A_IW_GRDH_1SDV_20210221T002752_20210221T002817_036681_044F80_B462	21/02/2021
S1A_IW_GRDH_1SDV_20220123T002758_20220123T002823_041581_04F21D_8083	23/01/2022
S1A_IW_GRDH_1SDV_20220204T002757_20220204T002822_041756_04F80B_BB59	04/02/2022
S1A_IW_GRDH_1SDV_20220216T002757_20220216T002822_041931_04FE36_72E1	16/02/2022

Table 2. Characteristics of SAR.

Polarization	VV/VH
Band	C(λ≈5.6 cm)
Raw spatial resolution	20 × 22 m (azimuths × ground range)
Square pixel spacing—Resampled	10 × 10 m (azimuths × ground range)
Swath width	250 km
Incidence angle range	$\sigma = 29.1^\circ - 46^\circ$
Format	GRD

Herein, the preprocessing protocol was applied according to the steps proposed by [38] [39], excluding the multi-look operation. GEE and the SNAP software were specifically used, and details of the operations performed are given below.

- **Radiometric calibration**: this step converts backscatter intensity as received by the sensor, to the normalized radar cross-section (σ^0), using the look-up-table (LUT) (A_σ) method, through the following relation (Equation (1)):

$$\sigma^0 = \frac{DN^2}{A_{dn}^2 \cdot K} \cdot \sin(\alpha) \Rightarrow A_\sigma = \sqrt{\frac{A_{dn}^2 \cdot K}{\sin(\alpha)}} \tag{1}$$

where, DN, is the digital number, A_{dn}, is the product of final scaling from internal to final or GRD, α, is the incidence angle, and K, is the calibration constant built-in the LUT A_σ, just provided for completeness. The output enables the comparison of different dates, sensors, or imaging geometries.

- **Speckle filtering or despeckling**: this step refers to reducing any random constructive/destructive interference, which results in salt and pepper noise throughout the image. The Refined Lee filter (RLF) was used, as it is designed to eliminate speckle noise while preserving edges and point features in SAR imagery [40]. The multiplicative noise model uses the Minimum Mean Square Error (MMSE) criterion to produce a smoothed pixel, following the expression (Equation (2)):

$$\hat{I}_{(x,y)} = \bar{I}_s + k_s\left(I_{(x,y)} - \bar{I}_s\right) \tag{2}$$

where, $\bar{I}_s$ is the mean value of the intensity within the filter window η_s, and k_s is the adaptive filter coefficient (More details with [40]).

- **Terrain flattening**: also known as range Doppler terrain correction, this operation corrects SAR geometric distortions such as, foreshortening, layover and shadow, by using the digital elevation model (DEM). The geocoding background process simultaneously converts the SAR image from slant range or ground range geometry, into a map coordinates system, which is here, the projection system, Universal Transverse Mercator (UTM), and the datum, World Geodetic System-1984 (WGS84).

The output has been used as main input data for the flood modelling.

2.3.2. Digital Elevation Model (DEM) Data

The "slope" layer in percent was selected from the watershed layer HydroSHEDS (V1-level 12), produced from a void filled Shuttle Radar Topographic Mission, SRTM-DEM, which has 1 arc-second spatial resolution, *i.e.*, approximately 30 meters. It was then used for the flood modelling. The "elevation" layer was also selected for location purpose, as well as to produce topography layers such as, contours, valley depth, channel network distance and relative slope position, for further validation. SAGA-GIS and ArcGIS integrated tools were specifically used here.

2.3.3. Optical Data

The Global Surface Water (JRC v1.3), produced from Landsat 5, 7 and 8 sensors, at 30 m of spatial resolution, was loaded on the GEE platform. The layer "seasonality", which corresponds to three decades of extraction and validation upon global permanent surface waters, was selected to proceed with the flood modeling. It specifically helps to separate perennial and extra surface waters.

Further, the Copernicus Global Land Service (CGLS) data (v3.0.1) at 100 m of spatial resolution was loaded to preview land use land cover (LULC) of the subset. The most updated freely available version is from year 2019. The GEE median reducer function was appended as the pixel-wise computation of the whole year to reduce the image collection, and the "urban-cover fraction" layer was selected. This helped to assess flood risk on human settlements.

Furthermore, the Sentinel2-Multispectral instrument (MSI) images were loaded in GEE interface. At mid-latitudes, the sensors collect near-nadir high resolution imagery on a 5-day revisit period for the constellation under cloud-free conditions, which results in 2 - 3-day revisit period, at a spatial resolution ranging from, 10 to 60 m. The cloud cover as well as date filters were applied to reduce the collection, by selecting images with the lowest atmospheric artefacts (cloud cover < 10%), in-between the targeted snowy period of year 2022 (**Table 3**). They were all obtained as Level-1C products from top-of-atmosphere (TOA) spectral reflectance, radiometrically and geometrically corrected, then the surface reflectance was simulated using the model proposed by [41]. Spectral bands with 20 m spatial resolution were rescaled at 10 m, before computing the tasseled cap transformation wetness (TCTw) and albedo layers (see Section 2.4.2). From the thirteen bands recording data in visible and infrared spectrum, only six were used according to the operation to be performed (**Table 4**).

Table 3. Identification of MSI (GEE JSON's format).

Granule ID	Acquisition
S2/20220129T171539_20220129T171910_T14SPB	29/01/2022
S2/20220205T170459_20220205T170741_T14SPB	05/02/2022
S2/20220208T171449_20220208T171931_T14SPB	08/02/2022

Table 4. Characteristics of MSI.

Spectral bands used	Blue (2), Green (3), Red (4), Narrow NIR (8A), SWIR1 (11), SWIR2 (12)
Spatial resolution	Blue (10), Green (10), Red (10), Narrow NIR (20), SWIR1 (20), SWIR2 (20)
Wide-swath	290 km
Type	Level-1C/TOA
Format	Tiff

Moreover, the newly released Landsat 9, Operation Land Imager 2-Thermal Infrared Sensors 2 (OLI-2/TIRS-2)[6], was loaded to compute land surface temperature (LST). This sensor collects near-nadir high resolution imagery for 16-day repeat cycle, at a spatial resolution ranging from 15 to 100 m, and images of Level-1 Precision Terrain (L1TP) data that have been well-characterized radiometry and are inter-calibrated at TOA spectral reflectance. The same selection and preprocessing scripts as above were applied to stay with low artefacts and inside the targeted timeline. Then, the multispectral image was subject to the pan-sharpening operation with panchromatic band to improve the spatial resolution at 15 m, using a simplified version of the code proposed by [42] in four steps: 1) sliding the window to form a mean array, 2) recording the variation from multispectral mean to panchromatic mean, 3) recording the variation of multispectral information from original to mean, 4) reassigning multispectral information into 15 m pixels by multiplying pan-band and two variations in each pixel.

In addition, the thermal infrared band 10, was converted to TOA spectral radiance (L_λ) and then at-satellite brightness temperature (T_B), using Equations (3) and (4) [43]:

$$L_\lambda = M_L \times \varphi_{cal} + A_l - Q_i \left(\text{watts}/\left(\text{m}^2 \cdot \text{s} \cdot \text{rad} \cdot \mu\text{m}\right)\right) \quad (3)$$

$$T_B = \frac{K_2}{L_n\left[\frac{K_1}{L_\lambda} + 1\right]} - 273.15\left({}^\circ\text{C}\right) \quad (4)$$

where, M_L and A_L are the specific multiplicative and additive rescaling factors (metadata file), K_1 and K_2 are the first and the second calibration con-

[6]https://web.archive.org/web/20170407145645/https://landsat.gsfc.nasa.gov/landsat-9/instruments/landsat-9-science-instrument-details/

stants (metadata file), while, **−273.15**, is the absolute zero value enabling the conversion of the output from the radiant temperature in Kelvin (**K**) to Celsius degree (˚C). The output was also rescaled at 15m to match the previous multispectral spatial resolution, then ready for the LST computation (see Section 2.4.2).

Table 5 and Table 6 give details of the Landsat 9 characteristics.

Above all preprocessing, some spatial resolution adjustment operations were performed, to enable a smooth transition among pixels and uniformize the outputs. Accordingly, layers were subject to upscaling and downscaling depending on the layer. Then final outputs were set at 10 m for the flooding (SAR original resolution), 10 m for TCTw and albedo (MSI/Stacked original resolution), and 15 m for LST (OLI/multispectral pan-sharpened resolution).

2.4. Core Processing

2.4.1. Flood Modelling

The thresholding method was combined to the change detection principle for this purpose. As first step, histograms distribution of the filtered and normalized, [0 - 1], SAR images, were found bimodal and analyzed to define thresholds among white and black bodies (Figure 5). Then, the preliminary floodwater extent was calculated by dividing the "before-event" image by the "after-event" one. After simulations, it was measured that, the three images shared the same threshold, **0.25**, for all the periods (Figure 5).

Table 5. Identification of Landsat 9 images (GEE JSON's format).

Scene ID	Acquisition
LC09/C02/T1/LC09_027037_20220104	04/01/2022
LC09/C02/T1/LC09_027037_20220205	05/02/2022
LC09/C02/T1/LC09_027037_20220309	09/03/2022

Table 6. Characteristics of Landsat 9.

Spectral bands stacked	Blue (2), Green (3), Red (4), NIR (5), SWIR1 (6), SWIR2 (7), Panchromatic (8)
Spatial resolution	Blue to SWIR2 (30), Panchromatic (15)
Wide-swath	185 km
Type	Level-1C/TOA
Format	Tiff

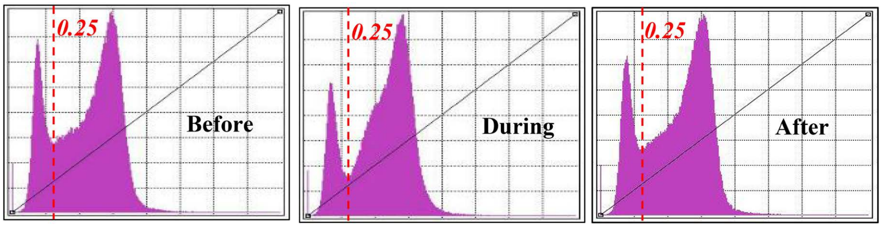

Figure 5. First threshold preview for the scenario of year 2022.

From there, the image change, expressed as a symmetric relative difference, was performed, using Equation (5):

$$FE = \left(\frac{T_2 - T_1}{|T_1|} + \frac{T_2 - T_1}{|T_2|} \right) \geq 0.25 \tag{5}$$

where, FE is the flood extent, T_1 is the image before, and T_2 is the image after event. Next step, using the JRC v1.3 data, a mask was applied on the perennial waters ("seasonality"), at a threshold **≥0.8**. Further, the percent slope was binarized, by using a cutoff value of **0.05**, because the area is a low-lying one. Then the preliminary floodwater extent was updated according to the slope threshold. Next, we proceed to an aggregation of pixels according to their distance and values. To do so, the GEE algorithm "ConnectedPixelCount" was used to remove unclustered pixels, at the threshold of **5**, and connect the **15** clustered pixels., At this point, a simple linear combination (SLC) with the urban layer from CGLS-v3.0.1, helped to identify human settlements exposed to the spotted flooding areas. Finally, using this output, the total flooded area was calculated.

2.4.2. Land Surface Short-Term Dynamics Characterization

Three operations were conducted here and their outputs used to proceed.

- **Tasseled cap transformation wetness (TCTw)**: it is the third axe amongst six principal components, and that has the specificity of highlighting soil surface moisture [44]. The general coefficients proposed for Sentinel2-MSI and inferred from Landsat8 OLI-TIRS ones by [45], were used as summarized in the following Equation (6):

$$\begin{aligned} \text{TCTW} = {} & 0.1509 \times \text{Band2} + 0.1973 \times \text{Band3} + 0.3279 \times \text{Band4} \\ & + 0.3406 \times \text{Band8A} - 0.7112 \times \text{Band11} - 0.4572 \times \text{Band12} \end{aligned} \tag{6}$$

- **Surface albedo**: it was computed still using Sentinel2-MSI, to express the local effective radiative forcing of the land surface and its impact on the contextual energy exchange. The formula uses the visible and infrared bands, with different sets of coefficients, and a constant, C, according to the weather's consequences on land cover [46]. Each equation was adapted in this study by using two constants (Equation (7) & (8)):

$$\begin{aligned} A_{SF} = {} & (0.5673 \times \text{Band2} + 0.1407 \times \text{Band3} + 0.2359 \times \text{Band4}) + C_1 \\ & + (0.5595 \times \text{Band8A} + 0.3844 \times \text{Band11} + 0.0290 \times \text{Band12}) + C_2 \end{aligned} \tag{7}$$

$$\begin{aligned} A_S = {} & (0.8421 \times \text{Band2} + 0.1487 \times \text{Band3} + 0.0088 \times \text{Band4}) + C_1 \\ & + (0.6793 \times \text{Band8A} + 0.0244 \times \text{Band11} + 0.6192 \times \text{Band12}) + C_2 \end{aligned} \tag{8}$$

where, A_{SF} and A_S, refer to the albedo snow-free and under snow, while C_1 and C_2 are the constants for the visible and the infrared broadbands. As such:

- For A_{SF}, $C_1 = -0.0048$ and $C_2 = -0.0073$;
- For A_S, $C_1 = -0.0052$ and $C_2 = -0.0221$.

- **Land surface temperature (LST)**: it was estimated by using the mono-window algorithm (MWA) [47]. This algorithm requires three parameters, *i.e.*, the effective mean atmospheric temperature (T_a), land surface emissivity (ε), and atmospheric transmittance (τ). The simplified expression for Landsat 9, TIR band 10, is the following (Equation (9)):

$$T_s = \left[a_{10}\left(1-C_{10}-D_{10}\right)+\left(b_{10}\left(1-C_{10}-D_{10}\right)+C_{10}+D_{10}\right)\times T_{10}-D_{10}T_a\right]/C_{10} \quad (9)$$

where, T_s, is the given Land surface Temperature, a_{10} and b_{10} are constants, and their values differ in different temperature ranges. Both C_{10} and D_{10} are functions of ε_{10} and τ_{10} in the following relations (Equations (10) & (11)):

$$C_{10} = \varepsilon_{10} \times \tau_{10} \quad (10)$$

$$D_{10} = \left(1-\tau_{10}\right)\times\left[1+\left(1-\varepsilon_{10}\right)\times\tau_{10}\right] \quad (11)$$

The effective mean atmospheric temperature, T_a, is approximated from the near surface air temperature (T_0) in linear relations depending on the atmosphere, while T_{10} is the corrected brightness temperature, *i.e.*, T_B. The detailed calculation and values of ε_{10} and τ_{10} are given as follows (Equations (12) & (13)) [48]:

$$\varepsilon_{10} = \varepsilon_{v\lambda}\mathrm{FVC}+\varepsilon_{s\lambda}\left(1-\mathrm{FVC}\right)+C_\lambda \quad (12)$$

$$\tau_{10} = -0.1146\omega+1.0256 \quad (13)$$

where, $\varepsilon_{v\lambda}$ and $\varepsilon_{s\lambda}$, represent the emissivity of vegetation and soil respectively, FVC, represents the fraction of vegetation cover, expressed as (Equations (14)):

$$\mathrm{FVC} = \left[\frac{\mathrm{NDVI}-\mathrm{NDVI}_{\min}}{\mathrm{NDVI}_{\max}-\mathrm{NDVI}_{\min}}\right]^2 \quad (14)$$

with,

$$\mathrm{NDVI} = \frac{\mathrm{NIR}\left(\mathrm{Band8}\right)-\mathrm{Red}\left(\mathrm{Band4}\right)}{\mathrm{NIR}\left(\mathrm{Band8}\right)+\mathrm{Red}\left(\mathrm{Band4}\right)} \quad (15)$$

Then, τ_{10}, expression is taken from the coefficients for the 1976 standard US atmospheric profile, from the relation between water vapor content, ω, and atmospheric transmittance, τ [48].

The whole methodology is described by three consecutive flowcharts composing **Figure 6**.

3. Results

3.1. Recurrently Flooded Areas and Urban's Exposure

It resulted from the flooding model that, the two events present similarities in statistics and spatial distribution. In 2021, an estimated 6.88 km^2 was flooded, based on the "After-Before" (melted snow) calculation (**Figure 7(A)**). Whereas, in 2022, the flooded (wet snow cover) area was 5.34 km^2 for the "During-Before" period, increasing to 6.85 km^2 for the "After-During" (melting snow) period, and 6.86 km^2 for the "After-Before" period (**Figure 7(A)**). Then, an important change is noticeable in the "During-Before" period, *i.e.*, 28.3% increase of flooded

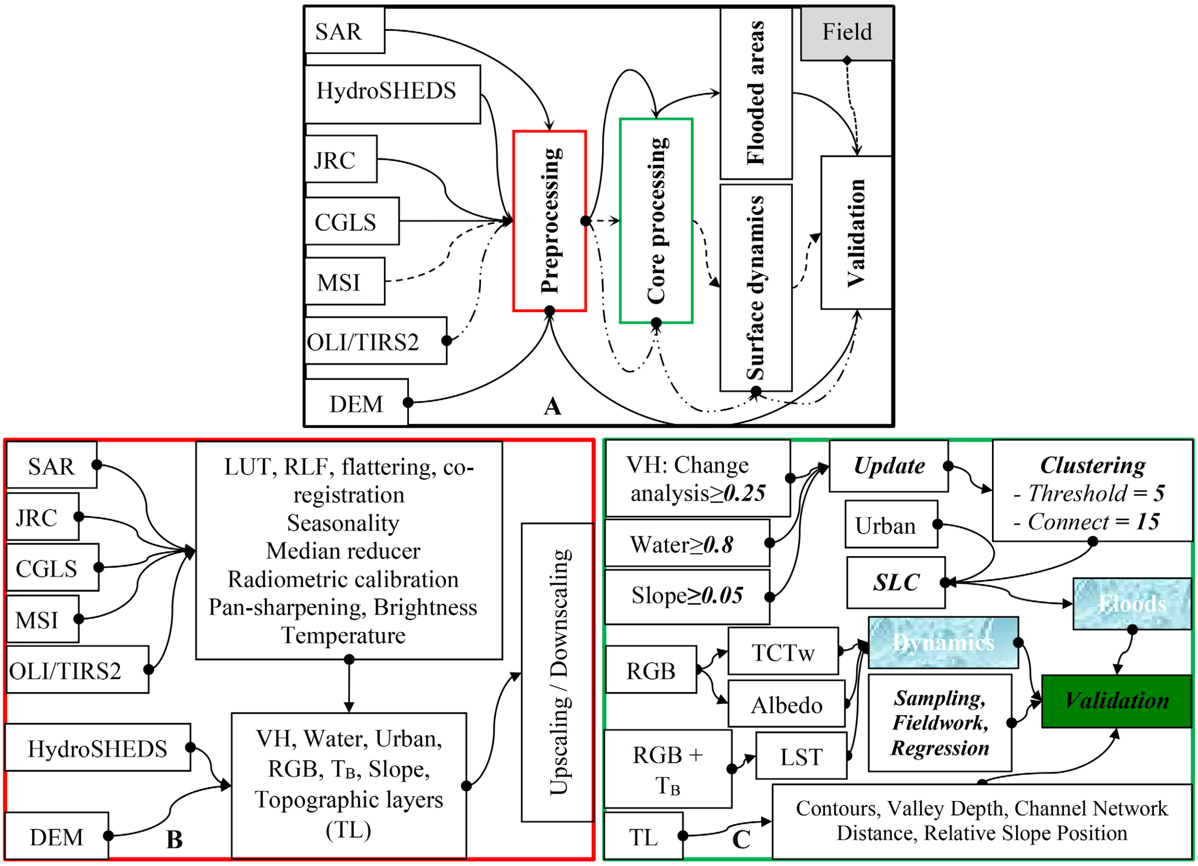

Figure 6. Flowchart of the methodology used in this study. (A) Simplified general dataflow diagram; (B) detailed steps of preprocessing; (C) detailed steps of the core processing.

area (wet snow cover). The after-snowmelt recurrently flooded areas were found distributed both on natural and urban land covers (Figure 7(B)).

In addition, as the "After-Before" outputs correspond to the melted snow or SWE, their crossing for the two years, revealed that they match over 5.65 km^2, *i.e.*, 2.4% of the study area (233.237 km^2). The resulting image represents the predicted after-snowmelt recurrently flooded area (Figure 7(B)). Further, the crossing of this last output with the urban layer (Figure 7(C)), resulted in 1.9 km^2 of predicted human settlements' exposed (35% of flooding area), while the remaining 3.7 km^2 (65% of flooding area) is occupied by the dominant natural features, *i.e.*, soils and vegetation (Figure 7(D) & Figure 7(E)).

3.2. Characteristics of Land Surface Dynamics

Globally as assumed, trends were found different before, during and after the snowfall-snowmelt. For a better assessment, the Sentinel2-MSI tile "Before" 2022 snowfall was used to sample one recurrently flooded pixel for wet vegetation, dry vegetation, wet soil and dry soil (Figure 8(A)). The calculated parameters, *i.e.*, TCTw, albedo and LST of the 2022 scenario were normalized, [0 - 1], and stacked. Then, the values of selected pixels per natural land features were recorded for comparison and further representation.

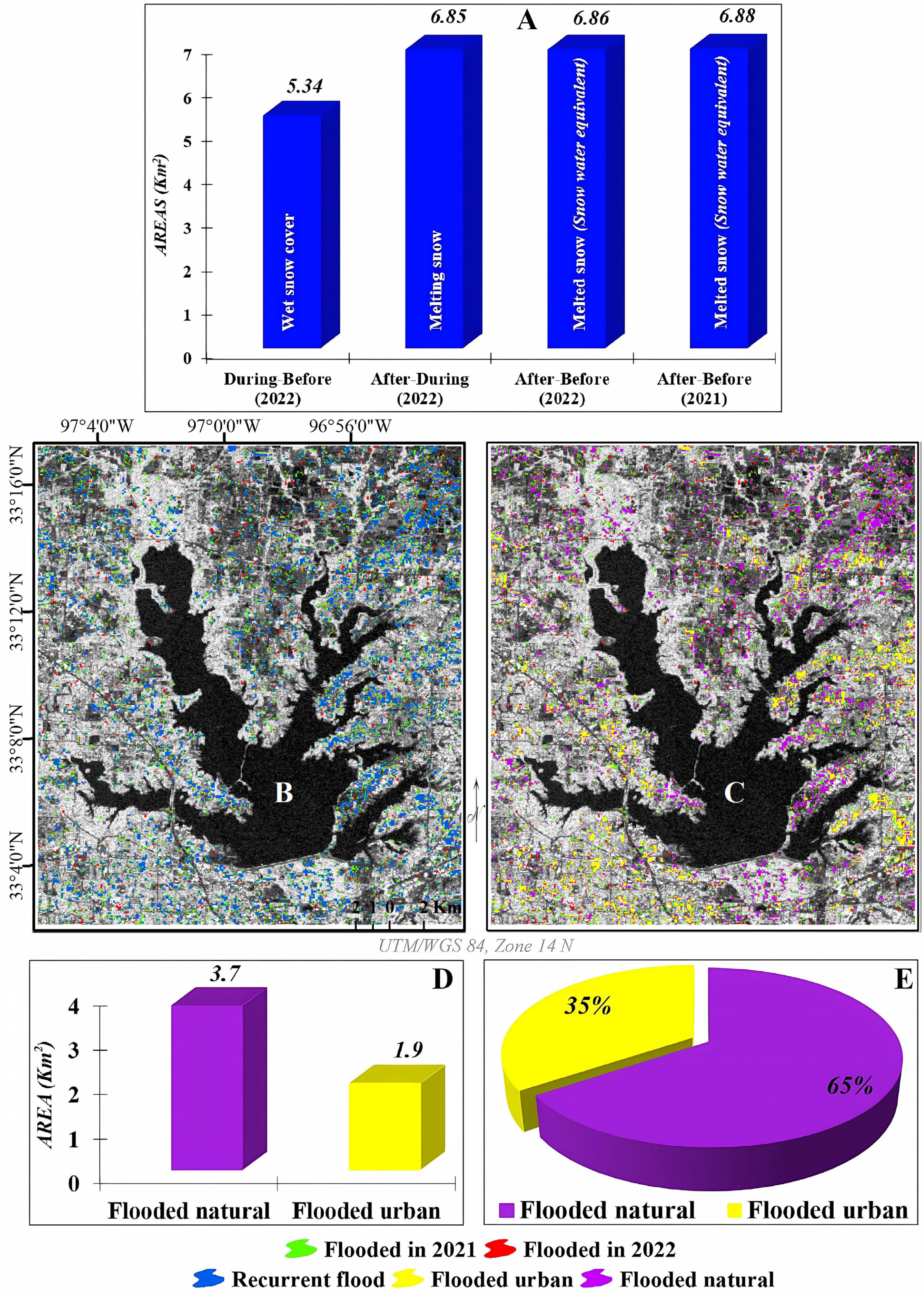

Figure 7. Flooded areas spatial and statistical distribution. (A) Snow flooded areas per event and period of the scenario; (B) 2021 and 2022 flooded areas spatial distribution displayed on after-snowmelt S1-SAR image of 2022; (C) result of the recurrently flooded areas extent with urban layer displayed on after-snowmelt S1-SAR image of 2022; D&E) Areas and ratios of recurrently flooded natural and urban features.

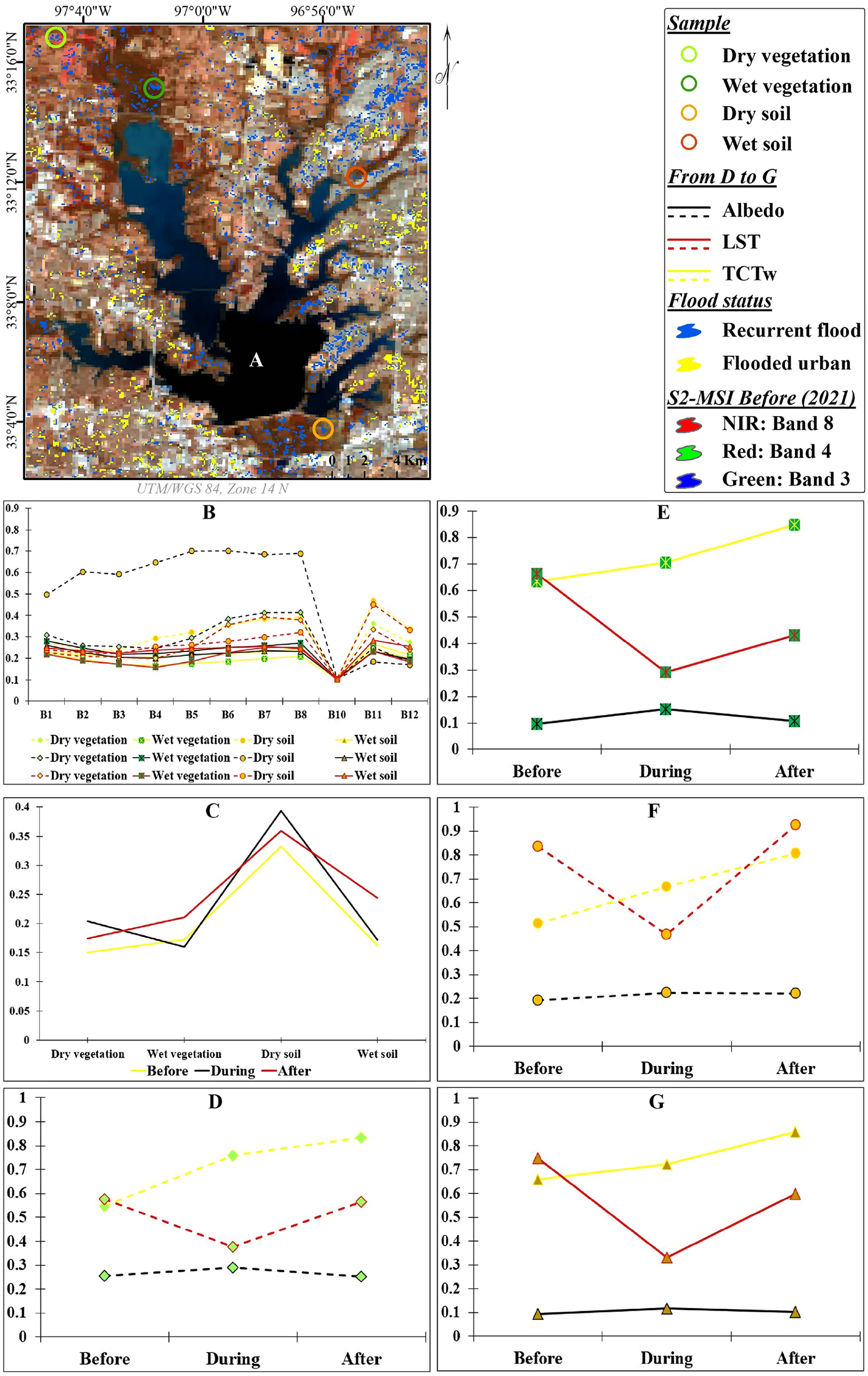

Figure 8. Land surface dynamics for vegetation and soil in 2022. (A) Sampling spots, recurrently flooded areas extent with urban, displayed on the MSI image of 2022; (B) spectral curves of land cover features; (C) parameters evolution for land cover features along the scenario; (D) dynamics of Parameters for dry vegetation; (E) dynamics of Parameters for wet vegetation; (F) dynamics of Parameters for dry soil; (G) dynamics of Parameters for wet soil.

Just as the spectral curves shows a clear difference among two samples of the same land cover (**Figure 8(B)**), trends of TCTw, albedo and LST presented more or less deviation one from another in general (**Figure 8(C)**). Single feature measures give details and more important differences that need to be raised.

Concerning dry vegetation, while albedo and LST contrasted at the "Before" and "After" period, they are converging in the "During" period of the scenario. Their curves vary between [0.2 - 0.6]. Whereas, the TCTw kept increasing and only became constant in the "After" period where the curve reaches 0.8 (**Figure 8(D)**). The exact dynamic of parameters was observed for wet vegetation, with more pronounced differences and divergences between albedo and LST. Likewise, the trends are identical for TCTw, but with a more pronounced increasing curve instead of the stabilization previously noticed in the "After" period, reaching up to 0.87 (**Figure 8(E)**).

When it comes to dry soil, LST is the most sensitive at each period of the scenario, with highest values in the "Before" (0.85) and "After" (0.93) periods above the other two parameters, and lowest values below the TCTw in the "During" period. Whereas, TCTw increases at all periods between [0.5 - 0.8], in contrast, albedo records the lowest changes as its values slightly fluctuate between [0.19 - 0.21] (**Figure 8(F)**). About wet soil, the same trends are observed, but with different values, that are lowest for LST ("Before": 0.75; "After": 0.61) and albedo (≈0.1), but highest for TCTw between [0.65 - 0.85] (**Figure 8(G)**).

Following the above, the summarizing assumption connects dynamics with high risk of flooding in the area, as discussed in the next section. Importantly, if changes in parameters for the vegetation cover and surroundings are to be considered from the aspect of roots for speed or rate of infiltration, soil on its side seems to be the more direct warning component, because dry or wet, it reacted more directly to water saturation, opposing more obviously trends of TCTw to LST, while showing small but not less important variations of albedo depending on the scale of the analysis.

4. Discussions

4.1. Summary (of) and Relationship (between) Findings

Overall, two main approaches were developed to achieve the two goals. The SAR image histogram display and thresholding helped to highlight waters. Then overtime, the image difference of SAR, updated by the thresholding perennial waters and slope layers, demarcated after-snowmelt additional waters from perennial ones for the study period, to define the recurrently flooded areas. In addition, land surface assessment approach proposed through three methods has been proven efficient in highlighting the differential between each period of the scenario. Therefore, the TCTw computed for S2-MSI was able to enhance land surface moisture differences. The proposed combination of albedo computation for the area with snow and snow-free has been able to assess the surface energy exchange during the scenario, although with less magnitudes than the other two components. Whereas, LST computation based on the mono-window algorithm, has been complementary to TCTw and albedo, as it is dependent on both moisture and surface energy. Nevertheless, since their values over the sampled land cover features, *i.e.*, soil and vegetation, described three different dynamics, they constitute assets each to another for the land surface dynamics in the scenario development.

From the above, water, soil and vegetation have been directly and easily highlighted in their spatial distribution as well as in their changes. Besides, the urban features, integrated from a different source (CGLS) and beforehand independent from the radar and optical data, has been interesting on both main outputs to assess human settlements exposure. As such, its crossing with flooded areas and display of the output on both raw SAR and S2-MSI images (**Figure 7** & **Figure 8**), was concluding for the best visualization of threats to the natural environment and to built-up areas. Further validations are supportive of methods as well as results.

4.2. Flood Map Validation

In absence of previous field records or geospatial related data, the recurrently flooded areas were display with three topographic layers plus contour values, *i.e.*, valley depth, channel network distance and relative slope position, for a laboratory validation and fieldwork verification. As such, the predicted at-risk areas fell outside of the Lewisville Lake's perennial waters area, and were distributed between medium and low values of valley depth (**Figure 9(A)**), corresponding to the small sand banks. Conversely, their distribution according to channel network distance (**Figure 9(B)**) and relative slope position (**Figure 9(C)**), is extended between medium and high values. Specifically, the far they are from the channel, and more comforting is the result showing that permanent surface waters

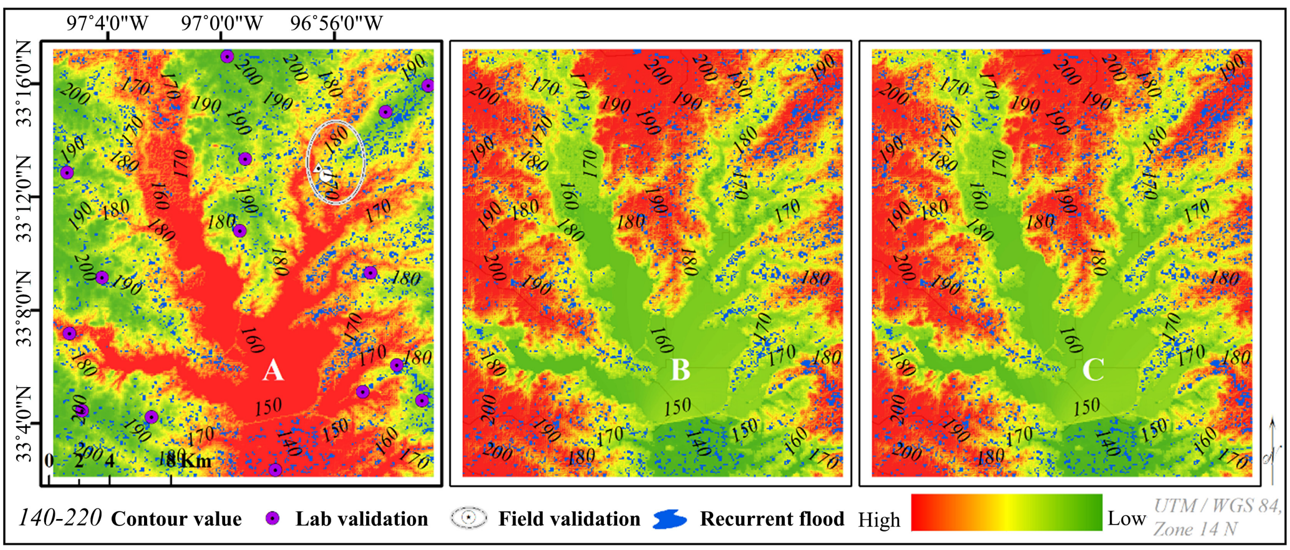

Figure 9. Flooded areas displayed on topographic layers most impacting the water stagnation. (A) Valley depth; (B) Channel network distance; (C) Relative slope position.

and temporal streams/rivers did not influence the analysis. As another supporting argument, it can be noticed that on 10 m equidistant contours, and a smooth denivelation of 80 m between ridges and gullies, flooding occurs almost everywhere between 150 m and 200 m, *i.e.*, bottoms of flat channels, small valleys and gutter interstices, which are suitable for water accumulation/stagnation.

Further, eighteen (18) flood points were randomly created in a cloud geodatabase referring to the perennial waters thresholded image. (See **Figure 9(A)**). The laboratory verification was conducted by displaying them on the Sentinel-1 image of "During" event of year 2022, and Sentinel-2 MSI image "Before" event of year 2021. By swiping and zooming, five over eighteen (5/18) points, *i.e.*, 27.8%, were confirmed recurrently flooded on built-up features. Eleven over eighteen (11/18) points, *i.e.*, 61.1% were recurrently flooded on natural features. These two groups represent 88.9% of the total flooded validation points (16/18). However, the two remaining (2/18), *i.e.*, 11.1%, failed in surrounding areas where ebbs and flows of Lewisville Lake perennial waters happen.

Complementarily, it was decided to focus on human settlements threats. Then, three over the five (3/5) points previously confirming urban flooded areas were selected for fieldwork verification. The fieldwork was conducted at "*Paloma Creek South*", a Census-Designated Place (CDP) in eastern Denton County, along highway "*US-380*" corridor. As result, two over three (2/3) points gave confirmation of built-up flooding, *i.e.*, 67%. Using the rule of three, it is up to 86.7% of the urban flooded validation points. Further, a random survey was conducted. At the "*Lake Trail access point#3*" by "*Shoreline Ridge Drive 400*" at 170m, the landscaping crew and residents confirmed that sand deposits on the walking paths are related to floodings and waters stagnation, which are clearly worst and longer during the winter, depending on snowfall amount and snowmelt speed. In the closest surroundings of that point, nearby houses' builders/owners adapted the foundation with stony walls, so to prevent further deterioration, infiltration and erosion (**Figure 10**, row1). This view was confirmed at the "*Lake Trail access point#5*" by "*Shoreline Ridge Drive Court*" at 164 m near the bridge, where sand deposits completely invaded the walking path and the fences, supported by the landscaping crew and residents' same testimony related to winter (**Figure 10**, row3). However, at the opposite of the latter, the residents of "*South Paloma Creek*" by "*Paloma Creek Boulevard*" at 176 m, never experienced a rainfall or snowmelt flood event (**Figure 10**, row2), all redirecting us to the areas around and adjacent "*Shoreline*" (*i.e.*, *Ridge Drive 400* and *Ridge Drive Court*).

4.3. Flood and Land Surface Short-Term Dynamics: What to Infer?

From existing studies, the computation of the "Before" and "After" normalized difference water index, NDWI [49], could be the easiest approach. The method used here is justified by the fact that Sentinel-2 MSI and Landsat images are randomly available, and usually with atmospheric artefacts (cloud/fog cover),

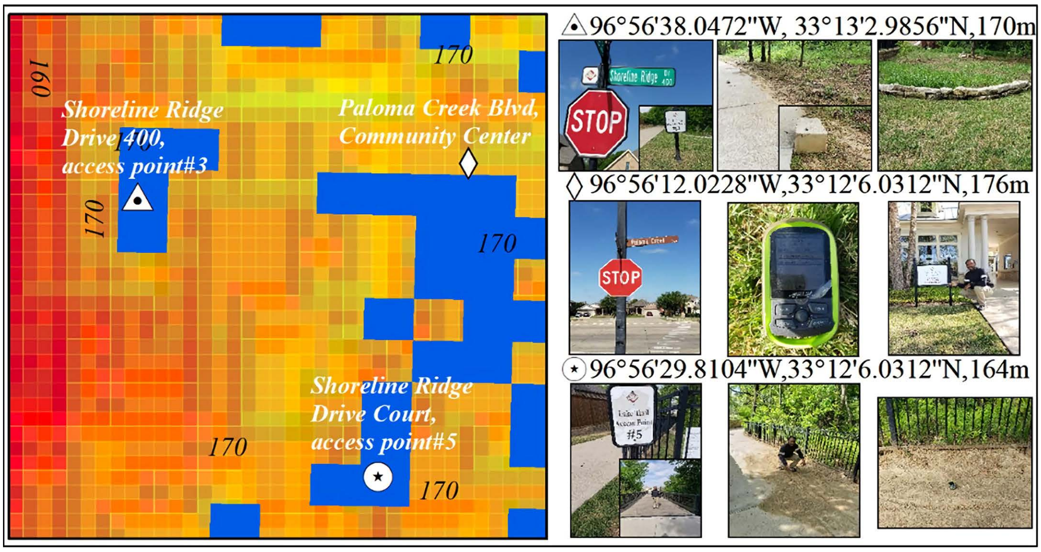

Figure 10. Results of fieldwork validation (April 18th, 2022). See supplemental material for additional pictures.

that considerably blur or totally cover the land surface during snowfalls and most part of the winter. Whereas, the revisit time of their sensors for each granule/scene (5-days and 16-days), may not exactly match the real-time "Before-During-After" snowfall scenario targeted in this study. Justifying then the approach used in this paper.

Concerning the post-analysis validation, the 2022 normalized layers, TCTw, albedo and LST of each period, were all crossed with the recurrently flooded layer to assess distribution and interactions. From outputs, the TCTw of each period has the highest influence on the flood spatial distribution and mostly after the snowmelt, with a total of 0.56 km^2. The albedo shows a balanced impact on each period (total = 0.38 km^2). While the LST of "During" (snowfall), better explains flooding, *i.e.*, wet snow extent (total = 0.37 km^2) (**Figure 11**). Therefore, the land surface dynamic indicators influence or are influenced by flooding (**Figure 12**).

However, the wetness seems to have a timeless impact, as validated with the polynomial regression conducted on land surface layers. This method has been successful in several studies, for instance the radiometric normalization [50], and the multi-temporal monitoring of crops [51]. A subset containing 2019 pixels, covering various dry and wet soil and vegetation, was extracted along the 2022 TCTw, albedo and LST layers of each period.

The fifth-order polynomial was concluded optimal for these samples, as the trend line was tested with same or decreasing value when the sixth-order was computed. As result, TCTw turns to be negatively correlated with both albedo and LST, before snowfall and after snowmelt, showing r-squares (R^2) between [0.54 - 0.82]. Whereas during snowfall, albedo is positively correlated with TCW (R^2 = 0.39) (**Figure 13**).

From the above, it can be assumed that wetness has the highest influence on

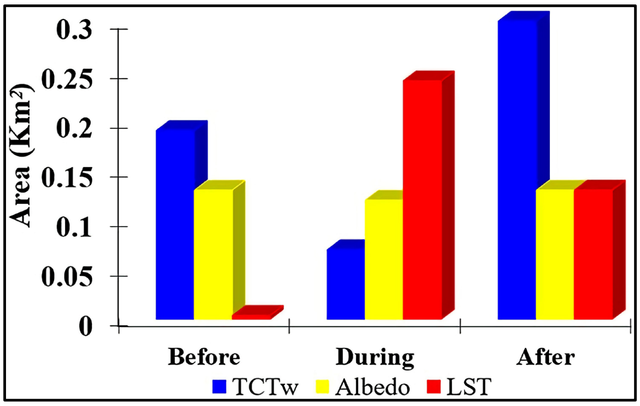

Figure 11. Flooded areas from the land surface dynamic parameters perspective.

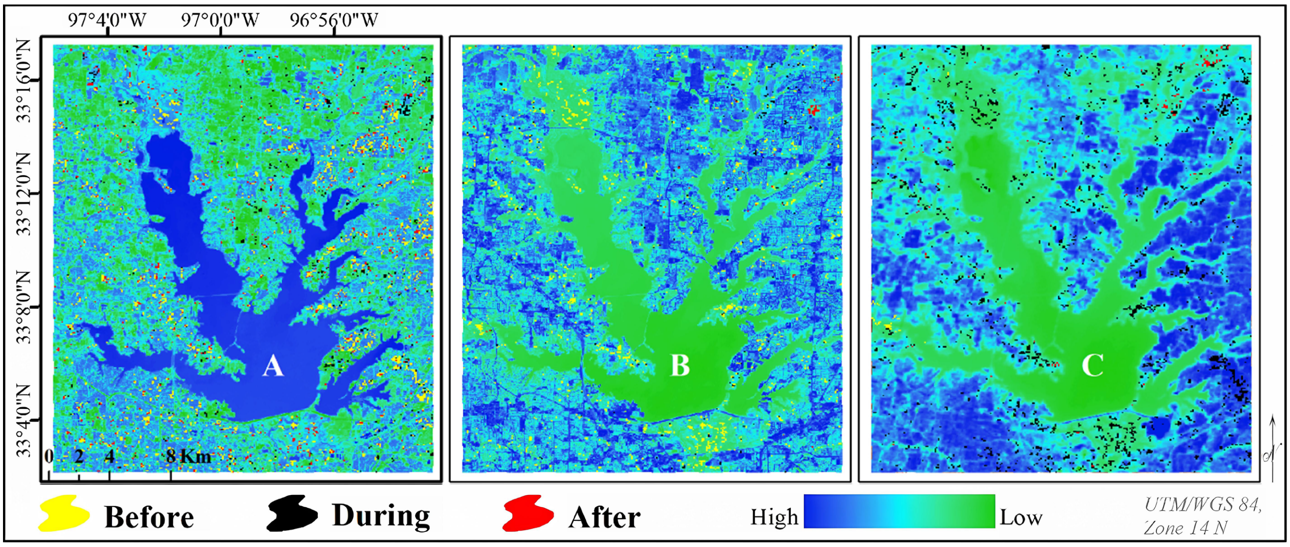

Figure 12. Flooded areas spotting from the land surface dynamic parameters perspective displayed on the 2022 after-snowmelt layers. (A) TCTW; (B) albedo; (C) LST.

land surface status at each step of a snowy event, and impacts seriously the distribution of albedo and LST. Moreover, TCW positive correlation with albedo in the "during" period and its highest negative correlation with LST ($R^2 = 0.68$) in the "after" period, illustrate the expansion of wetness on usually less or not concerned spots. As causality, it could then be inferred that with snowfall and snowmelt, the wetness increases and stays constant for a long time (the "after" image was acquired 13 days after the snowfall see Table 1), the surface energy is deeply lowered, while the surface temperature slowly increases back to the normal after the melting. All the previous happens with a direct impact on recurrent water stagnation and temporary flooding. Nevertheless, the level of stagnation is assumed to be different, according to soil porosity or impermeability, which has not been explicitly explored in this study.

4.4. Limitations and Caveats

The regression amongst LST and TCTw, is at some point exposed to accuracy

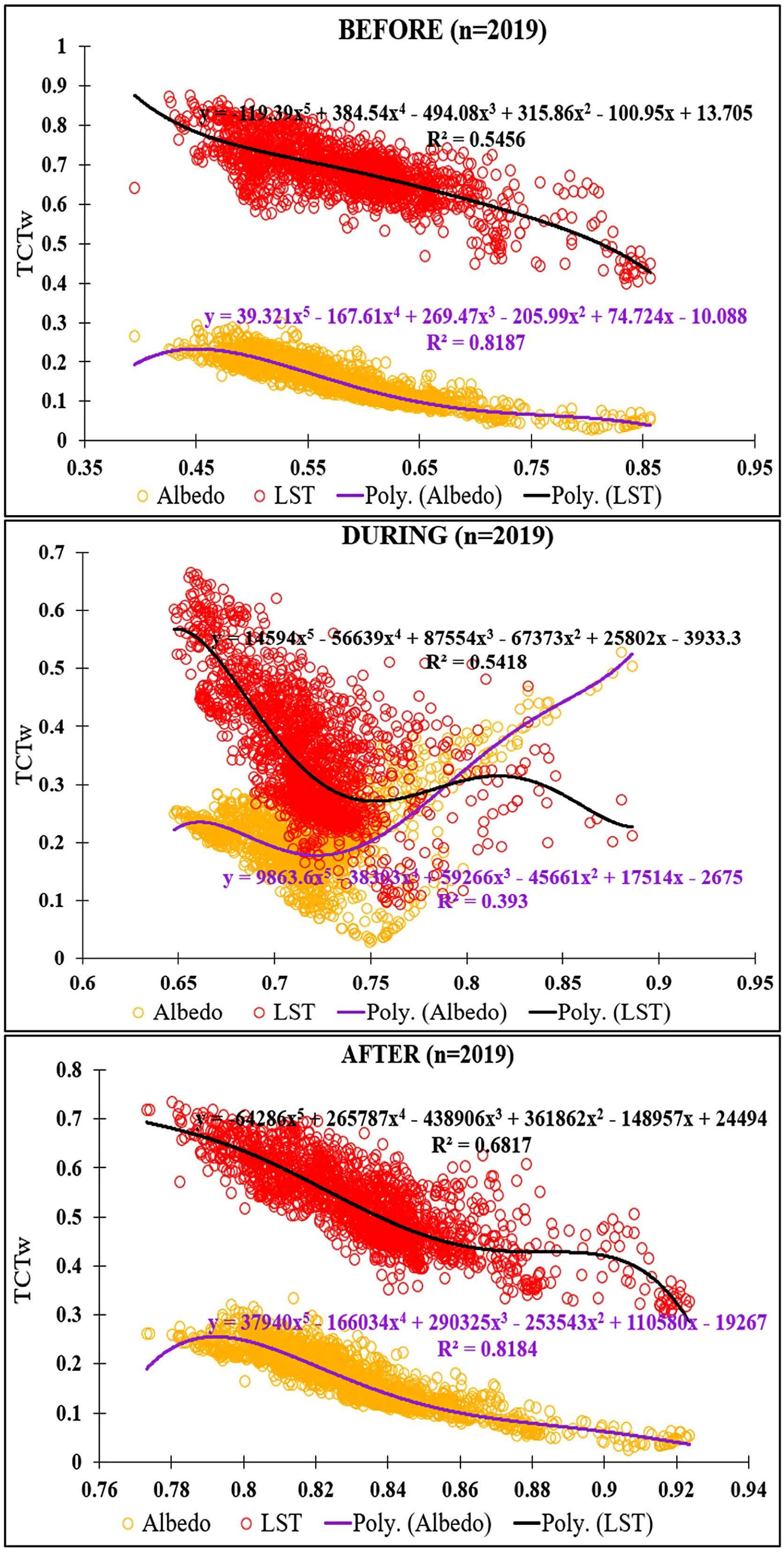

Figure 13. Fifth-order polynomial regression model.

biases. In fact, images of Landsat-9 used to produce LST have been available a month apart, while only the "During" event scene, recorded on February the 5th share the same conditions as Sentinel-2 granule (See **Table 1**). Although outputted trends are acceptable in the logic of the scenario analysis, pixels' value relation with the regression analysis might present some deviations, which were not pointed out. Computations under the optimal conditions absolutely need the same date scene and granule.

Moreover, the method still needs to be compared with other well-proven models. For instance, machine learning classifiers may be performed to proceed with a further assessment of land cover features, to validate the extent of snow-cover, as well as differentiate perennial waters from additional temporary water surface and new streams, that were created and sourced from Lewisville Lake according to DFW metropolitan urban needs. This would bring a different perspective to the accuracy assessment. Ongoing works will complete this step, adding potential further snowfalls.

5. Conclusions

To sum up, the geospatial knowledge of snowmelt impact in areas less regularly and deeply affected, but facing some unpredictable records of huge snowfalls, mays help for forecasting and warning system implementation. The methodology has relied on passive and active remotely sensed data, as well as pre-/post-analysis laboratory validation and fieldwork, for useful results ensuring locals' safety. About 5.6 km^2 correspond to recurrently flooded areas around the Lewisville Lake, whose 1.9 km^2 are urban. It was also assessed that the state of land surface dynamics is substantially important, with a constant increase of wetness, versus increased to abrupt changes in surface energy and temperature. The wetness especially was defined as the main driver or explainable variable of flooding, as TCTw matched 0.56 km^2 of recurrently flooded areas, and was always positively correlated with snowfalls, wet snow and snowmelt. Therefore, if snowmelt-related flooding has not yet been declared as a proper human threat in the study area to the best of our knowledge, it seems important that the urban planning, *i.e.*, built-up expansion and new cities creation, in Denton County, takes these forecasting into consideration.

Finally, the ongoing experimentations are directed towards addressing the limitations above mentioned. For now, the team plans to collect more closely available satellite data for the same dates to restart a scenario for upcoming events. In addition, the thresholding approach which is a simple straightforward method, is being compared with the NDWI computation from optical data as well as artificial intelligence methods, especially machine learning. Moreover, the fieldwork is intended to cover at least 30% of the sampling, as advised in the literature. This might help the improvement of future outcomes, in better preventing and mitigating unexpected snowfall-snowmelt hazard exposure, when recalling the "*snowpocalypse*" of February 10th, of 2010.

Acknowledgements

To Google Earth Engine experts-developers for multiple APIs freely available.

To USGS for freely available data. To landscaping crew and residents of Paloma Creek South for the assistance and interaction during fieldwork validation. To StatsN'Maps Consulting Firm, for the logistic, financial and technical support.

Fundings

The private consulting firm StatsN'Maps, through its "Research Support Funds" (SN'M-RSF), financially supported the purchase of articles and book chapters on sale, as well as all the fieldwork investigations for complementary data acquisition. The licensed software, Erdas Imagine version 16.6.0.1366, ArcGIS version 10.8.2, SAGA-GIS version 8.0.1, and XLStats version 2020.1.64570, used in this research are properties of StatsN'Maps and available upon request.

Conflicts of Interest

The authors declare no conflicts of interest regarding the publication of this paper.

References

[1] Marks, D., and Dozier, J. (1992) Climate and Energy Exchange at the Snow Surface in the Alpine Region of the Sierra Nevada: 2. Snow Cover Energy Balance. *Water Resources Research*, **28**, 3043-3054. https://doi.org/10.1029/92WR01483

[2] Henderson, G.R., Peings, Y., Furtado, J.C. and Kushner, P.J. (2018) Snow-Atmosphere Coupling in the Northern Hemisphere. *Nature Climate Change*, **8**, 954-963. https://doi.org/10.1038/s41558-018-0295-6

[3] Kimball, J.S., Du, J., Pan, C., Rawlins, M., Kirchner, P., Yi, Y., Kim, Y., Park, H. and Derksen, C. Remote Sensing of Snow Phenology. https://www.ntsg.umt.edu/project/remote-sensing-snow.php

[4] Hall, D.K., Riggs, G.A. and Salomonson, V.V. (1995) Development of Methods for Mapping Global Snow Cover Using Moderate Resolution Imaging Spectroradiometer Data. *Remote Sensing of Environment*, **54**, 127-140. https://doi.org/10.1016/0034-4257(95)00137-P

[5] Hall, D.K., Riggs, G.A., Salomonson, V.V., Digirolamo, N.E. and Bayr, K.J. (2002) MODIS Snow-Cover Products. *Remote Sensing of Environment*, **83**, 181-194. https://doi.org/10.1016/S0034-4257(02)00095-0

[6] Salomonson, V.V. and Appel, I. (2004) Estimating Fractional Snow Cover from MODIS Using the Normalised Difference Snow Index. *Remote Sensing of Environment*, **89**, 351-360. https://doi.org/10.1016/j.rse.2003.10.016

[7] Nolin, A.W., Dozier, J. and Mertes, L.A.K. (1993) Mapping Alpine Snow Using a Spectral Mixture Modelling Technique. *Annals of Glaciology*, **17**, 121-124. https://doi.org/10.3189/S0260305500012702

[8] He, G., Feng, X., Xiao, P., Xia, Z., Wang, Z., Chen, H., Li, H. and Guo, J. (2017) Dry and Wet Snow Cover Mapping in Mountain Areas Using SAR and Optical Remote Sensing Data. *IEEE Journal of Selected Topics in Applied Earth Observations and Remote Sensing*, **10**, 2575-2588. https://doi.org/10.1109/JSTARS.2017.2673409

[9] Snapir, B., Momblanch, A., Jain, S.K., Waine, T.W. and Holman, I.P. (2019) A Method for Monthly Mapping of Wet and Dry Snow Using Sentinel-1 and MODIS: Application to a Himalayan River Basin. *International Journal of Applied Earth Ob-*

servation and Geoinformation, **74**, 222-230. https://doi.org/10.1016/j.jag.2018.09.011

[10] Tsai, Y.-L.S., Dietz, A., Oppelt, N. and Kuenzer, C. (2019) Wet and Dry Snow Detection Using Sentinel-1 SAR Data for Mountainous Areas with a Machine Learning Technique. *Remote Sensing*, **11**, Article No. 895. https://doi.org/10.3390/rs11080895 https://www.mdpi.com/2072-4292/11/8/895

[11] Flanner, M.G. and Zender, C.S. (2006) Linking Snowpack Microphysics and Albedo Evolution. *Journal of Geophysical Research*, **111**, Article No. D12208. https://doi.org/10.1029/2005JD006834

[12] Gouttevin, I., Menegoz, M., Dominé, F., Krinner, G., Koven, C., Ciais, P., Tarnocai, C., and Boike, J. (2012) How the Insulating Properties of Snow Affect Soil Carbon Distribution in the Continental Pan-Arctic Area. *Journal of Geophysical Research*, **117**, Article No. G02020. https://doi.org/10.1029/2011JG001916

[13] Le Toumelin, L., Amory, C., Favier, V., Kittel, C., Hofer, S., Fettweis, X., Gallée, H. and Kayetha V. (2021) Sensitivity of the Surface Energy Budget to Drifting Snow as Simulated by MAR in Coastal Adelie Land, Antarctica. *The Cryosphere*, **15**, 3595-3614. https://doi.org/10.5194/tc-15-3595-2021

[14] Hansen, J. and Nazarenko, L. (2004) Soot Climate Forcing via Snow and Ice Albedos. *Proceedings of the National Academy of Sciences of the United States of America*, **101**, 423-428. https://doi.org/10.1073/pnas.2237157100

[15] Qu, X. and Hall, A. (2014) On the Persistent Spread in Snow-Albedo Feedback. *Climate Dynamics*, **42**, Article No. L03502. https://doi.org/10.1007/s00382-013-1774-0

[16] Liang, S. (2001) Narrowband to Broadband Conversions of Land Surface Albedo I: Algorithms. *Remote Sensing of Environment*, **76**, 213-238. https://doi.org/10.1016/S0034-4257(00)00205-4

[17] Schaaf, C.B., *et al.* (2002) First Operational BRDF, Albedo Nadir Reflectance Products from MODIS. *Remote Sensing of Environment*, **83**, 135-148. https://doi.org/10.1016/S0034-4257(02)00091-3

[18] Stroeve, J., Box, J.E., Gao, F., Liang, S., Nolin, A. and Schaaf, C. (2005) Accuracy Assessment of the MODIS 16-Day Albedo Product for Snow: Comparisons with Greenland in Situ Measurements. *Remote Sensing of Environment*, **94**, 46-60. https://doi.org/10.1016/j.rse.2004.09.001

[19] Thiebault, K. and Young, S. (2020) Snow Cover Change and Its Relationship with Land Surface Temperature and Vegetation in Northeastern North America from 2000 to 2017. *International Journal of Remote Sensing*, **41**, 8453-8474. https://doi.org/10.1080/01431161.2020.1779379

[20] Marchand, N., Royer, A., Krinner, G., Roy, A., Langlois, A. and Vargel, C. (2018) Snow-Covered Soil Temperature Retrieval in Canadian Arctic Permafrost Areas, Using a Land Surface Scheme Informed with Satellite Remote Sensing Data. *Remote Sensing*, **10**, Article No. 1703. https://doi.org/10.3390/rs10111703

[21] Peng, S., Piao, S., Ciais, P. and Fang, J. (2010) Change in Winter Snow Depth and Its Impacts on Vegetation in China. *Global Change Biology*, **16**, 3004-3013. https://doi.org/10.1111/j.1365-2486.2010.02210.x

[22] Manickam, S. and Barros, A. (2020) Parsing Synthetic Aperture Radar Measurements of Snow in Complex Terrain: Scaling Behaviour and Sensitivity to Snow Wetness and Landcover. *Remote Sensing*, **12**, Article No. 483. https://doi.org/10.3390/rs12030483

[23] Wang, S., Zhou, F. and Russell, H.A.J. (2017) Estimating Snow Mass and Peak River Flows for the Mackenzie River Basin Using GRACE Satellite Observations. *Remote Sensing*, **9**, Article No. 256. https://doi.org/10.3390/rs9030256

[24] Hussainzada, W., Lee, H.S., Vinayak, B. and Khpalwak, G.F. (2021) Sensitivity of Snowmelt Runoff Modelling to the Level of Cloud Coverage for Snow Cover Extent from Daily MODIS PRODUCT COLLEction 6. *Journal of Hydrology*: *Regional Studies*, **36**, Article ID: 100835. https://doi.org/10.1016/j.ejrh.2021.100835

[25] Largeron, C., Dumont, M., Morin, S., Boone, A., Lafaysse, M., Metref, S., Cosme, E., Jonas, T., Winstral, A. and Margulis, S.A. (2020) Toward Snow Cover Estimation in Mountainous Areas Using Modern Data Assimilation Methods: A Review. *Frontiers in Earth Science*, **8**, Article 325. https://doi.org/10.3389/feart.2020.00325

[26] Nolin, A.W. (2010) Recent Advances in Remote Sensing of Seasonal Snow. *Journal of Glaciology*, **56**, 1141-1150. https://doi.org/10.1080/15481603.2021.1946938

[27] Pan, C.G., Kimball, J.S., Munkhjargal, M., Robinson, N.P., Tijdeman, E., Menzel, L. and Kirchner, P. (2019) Role of Surface Melt and Icing Events in Livestock Mortality across Mongolia's Semi-Arid Landscapes. *Remote Sensing*, **11**, Article No. 2392. https://doi.org/10.3390/rs11202392

[28] DeWalle, D.R. and Rango, A. (2008) Principles of Snow Hydrology. Cambridge University Press, Cambridge, 410 p. https://doi.org/10.1017/CBO9780511535673

[29] Butt, M.J. and Bilal, M. (2011) Application of Snowmelt Runoff Model for Water Resource Management. *Hydrological Processes*, **25**, 3735-3747. https://doi.org/10.1002/hyp.8099

[30] Bomar, G.W. (1983) Texas Weather. University of Texas Press, Austin, 265 p.

[31] InFRM (2021) Interagency Flood Risk Management (InFRM): Watershed Hydrology Assessment for the Trinity River Basin. https://webapps.usgs.gov/infrm/pubs/InFRM%20Trinity%20WHA%20Report%20July2021.pdf

[32] Banks, K. (2008) Control of Nonpoint Source Loads in the Hickory Creek Sub-Basin of the Lake Lewisville Watershed as a Component of a Watershed-Based Water Quality Trading Program. *Report*, 210 p. https://www.cityofdenton.com/DocumentCenter/View/596/Hickory-Creek-Watershed-Protection-Plan-PDF

[33] Gorelick, N., Hancher, M., Dixon, M., Ilyushchenko, S., Thau, D. and Moore, R. (2017) Google Earth Engine: Planetary-Scale Geospatial Analysis for Everyone. *Remote Sensing of Environment*, **202**, 18-27. https://doi.org/10.1016/j.rse.2017.06.031

[34] Dietz, A.J., Kuenzer, C., Gessner, U. and Dech, S. (2012) Remote Sensing of Snow—A Review of Available Methods. *International Journal of Remote Sensing*, **33**, 4094-4134. https://doi.org/10.1080/01431161.2011.640964

[35] CEOS/GFOI (2018) A Layman's Interpretation Guide to L-Band and C-Band Synthetic Aperture Radar Data. Version 2.0. https://ceos.org/publications/a-laymans-interpretation-guide-to-l-band-and-c-band-synthetic-aperture-radar-data/

[36] Grody, N.C. and Basist, A.N. (1996) Global Identification of Snow Cover Using SSM/I Measurements. *IEEE Transactions on Geoscience and Remote Sensing*, **34**, 237-249. https://doi.org/10.1109/36.481908

[37] Amlien, J. (2008) Remote Sensing of Snow with Passive Microwave Radiometers. A Review of Current Algorithms. *Report*, 1019 (Oslo: Norsk Regnesentral). https://nr.no/en/publication/958059/

[38] Nuno, M. and Meadows, P.J. (2015) Radiometric Calibration of S-1 Level-1 Products Generated by the S-1 IPF. European Spatial Agency, Paris, 13 p. https://sentinels.copernicus.eu/documents/247904/685163/S1-Radiometric-Calibration-V1.0.pdf

[39] Braun, A. and Veci, L. (2021) Sentinel-1 Toolbox TOPS Interferometry Tutorial. Tutorial, 25 p. https://pdf4pro.com/amp/view/sentinel-1-toolbox-tops-interferometry-tutorial-7363e6.html

[40] Li, H., Huang, B. and Huang, X. (2010) A Level Set Filter for Speckle Reduction in SAR Images. *EURASIP Journal on Advances in Signal Processing*, **2010**, Article No. 745129. https://doi.org/10.1155/2010/745129

[41] Chavez Jr., P.S. (1996) Image-Based Atmospheric Corrections—Revisited and Improved. *Photogrammetric Engineering and Remote Sensing*, **62**, 1025-1036. http://static1.1.sqspcdn.com/static/f/891472/15133582/1321370214637/Chavez_P.S._1996.pdf?token=z0vrMkYqCcjZKksJLZYfRnYFSRc%3D

[42] Dong, Y., Ren, Z., Fu, Y., Miao, Z., Yang, R., Sun, Y. and He, X. (2020) Recording Urban Land Dynamic and Its Effects during 2000-2019 at 15-m Resolution by Cloud Computing with Landsat Series. *Remote Sensing*, **12**, Article No. 2451. https://doi.org/10.3390/rs12152451

[43] USGS (2019) Landsat 8 (L8) Data Users Handbook. LDSD-1574, Version 5.0. 114 p. https://www.usgs.gov/landsat-missions/landsat-8-data-users-handbook

[44] Kauth, R.J. and Thomas, G.S. (1976) The Tasselled Cap—A Graphic Description of the Spectral-Temporal Development of Agricultural Crops as Seen by Landsat. *Proceedings of the Symposium on Machine Processing of Remotely Sensed Data*, West Lafayette, 1 January 1976, 4B41-4B51. https://citeseerx.ist.psu.edu/viewdoc/download?doi=10.1.1.461.6381&rep=rep1&type=pdf

[45] Shi, T. and Xu, H. (2019) Derivation of Tasseled Cap Transformation Coefficients for Sentinel-2 MSI At-Sensor Reflectance Data. *IEEE Journal of Selected Topics in Applied Earth Observations and Remote Sensing*, **12**, 4038-4048. https://doi.org/10.1109/JSTARS.2019.2938388

[46] Li, Z., Erb, A., Sun, Q., Liu, Y., Shuai, Y., Wang, Z., Boucher, P. and Schaaf, C., (2018) Preliminary Assessment of 20-m Surface Albedo Retrievals from Sentinel-2A Surface Reflectance and MODIS/VIIRS Surface Anisotropy Measures. *Remote Sensing of Environment*, **217**, 352-365. https://doi.org/10.1016/j.rse.2018.08.025

[47] Qin, Z. and Karnieli, A. (2001) A Mono-Window Algorithm for Retrieving Land Surface Temperature from Landsat TM Data and Its Application to the Israel-Egypt Border Region. *International Journal of Remote Sensing*, **22**, 3719-3746. https://doi.org/10.1080/01431160010006971

[48] Rozenstein, O., Qin, Z., Derimian, Y., and Karnieli, A. (2014) Derivation of Land Surface Temperature for Landsat-8 TIRS Using a Split Window Algorithm. *Sensors*, **14**, 5768-5780. https://doi.org/10.3390/s140405768

[49] Gao, B.C. (1996) NDWI—A Normalized Difference Water Index for Remote Sensing of Vegetation Liquid Water from Space. *Remote Sensing of Environment*, **58**, 257-266. https://doi.org/10.1016/S0034-4257(96)00067-3

[50] Rahman, M.M., Hay, G.J., Couloigner, I., Hemachandran, B. and Bailin, J. (2014) An Assessment of Polynomial Regression Techniques for the Relative Radiometric Normalization (RRN) of High-Resolution Multi-Temporal Airborne Thermal Infrared (TIR) Imagery. *Remote Sensing*, **6**, 11810-11828. https://doi.org/10.3390/rs61211810

[51] Du, M.M., Noguchi, N., Itoh, A. and Shibuya, Y. (2017) Multi-Temporal Monitoring of Wheat Growth by Using Images from Satellite and Unmanned Aerial Vehicle. *International Journal of Agriculture and Biological Engineering*, **10**, 1-13. https://doi.org/10.25165/j.ijabe.20171005.3180

Supplemental Materials

Complementary fieldwork pictures. From left to right: Lyndon B Johnson Freeway at Hillcrest Plaza Drive, on February 14^{th}, 2021, 6:49 AM; Field Measures at Cottonwood Park in Richardson (2.7 inches); Another waypoint at Paloma Creek at a different altitude, where residents confirmed there has never been flood; Trace of floodings due to raising of Lewisville Lake added to snowmelt additional waters on a stony public bench of 0.6 meters at Shoreline Ridge Drive Court; Flooded areas in a wooded vegetation between the fences and the ridge at Lake Trail access point#5.